Effect of geometry on the downstream flow topology of a micro ramp in a supersonic turbulent boundary layer

An experimental study

Tambe, Sumit; Schrijer, Ferdinand; van Oudheusden, Bas

Publication date
2017

Document Version
Final published version

Published in
7th European Conference For Aeronautics And Space Sciences

Citation (APA)
Tambe, S., Schrijer, F., & van Oudheusden, B. (2017). Effect of geometry on the downstream flow topology of a micro ramp in a supersonic turbulent boundary layer: An experimental study. In *7th European Conference For Aeronautics And Space Sciences: Milan, Italy*

Effect of geometry on the downstream flow topology of a micro ramp in a supersonic turbulent boundary layer: an experimental study

S.S. Tambe, F.F.J. Schrijer and B.W. van Oudheusden
Faculty of Aerospace Engineering, Delft University of Technology, Netherlands

Abstract

The physical relation between the geometry and the flow topology of the wake of a micro ramp is investigated by means of a parametric study. Various micro ramp geometries are placed in a supersonic turbulent boundary layer at a free-stream Mach number of 2. The flow field is measured with schlieren and Particle Image Velocimetry (PIV). The effect of geometry on different aspects of the flow field is studied and from this a physical model of the flow phenomena is formulated. This model includes the concept of captured momentum, a simplified expression which allows relating the geometrical features to vortex circulation and from this a new scaling factor is proposed. The physical model is validated with the experimental data.

1. Introduction

The problem of boundary layer separation is crucial when designing complex aerospace systems for advanced air vehicles. In the case of transonic and supersonic vehicles, shock waves are common to occur which impose a sharp rise in the pressure. Upon interaction with such a shock-wave, the boundary layer encounters a strong adverse pressure gradient and becomes prone to separate. On a transonic wing, shock induced boundary layer separation can cause violent buffeting which puts limits on the flight envelope. Shock-Wave Boundary Layer Interaction (SWBLI) also occurs in the inlet of supersonic engines, where it may induce a separation bubble. Unsteadiness caused by such separation results in inlet buzz or may even lead to engine unstart. This problem is traditionally tackled by the application of a boundary layer bleed system where the low momentum flow near the wall is removed from the inlet. In order to compensate for the loss of mass flow through the bleed system, the size of the inlet is increased [1]. Also, depending on its implementation, bleed systems may require active components like pumps, valves etc. This makes this system bulky and complex causing a further reduction in fuel efficiency. Instead, the use of passive (net zero mass flux) flow control devices such as vortex generators is a potentially better solution, as their application is simple, robust and fail-safe [2], [3]. This makes the overall system light-weight and hence the overall drag penalty is reduced. Also, practical implementation of these devices is simple and requires less maintenance, which translates to reduced manufacturing and maintenance costs.

Vortex generator devices produce a pair of streamwise counter rotating vortices which enhance mixing in the downstream flow and draw higher momentum fluid near the wall. This results in a fuller boundary layer profile in the near-wall region, which can sustain higher adverse pressure gradients without having flow separation. Modern micro vortex generator (MVG) configurations differ from the more traditional ones, as they are fully submerged in the boundary layer and hence have a lower drag. Out of various types of micro vortex generator configurations, micro ramps produce the lowest drag and hence are an attractive choice for flow control [2]–[5].

Various studies have been performed to assess the effectiveness of micro ramps for flow control applications. The flow structure of the micro ramp wake has been explored in detail both computationally and experimentally [6]–[8]. The effects of Mach number, Reynolds number and device height on the various characteristics of the micro ramp wake have been addressed [1], [9]. Various micro ramp configurations have also been tested to mitigate shock induced separation [5]. However, in the whole research effort on micro-ramps the effect of the geometry on the downstream flow topology is only partially covered (typically only the so-called Anderson geometry [3] is

investigated). Thus, although there is a basic understanding of the physical relation between the micro ramp geometry and the downstream flow topology, there is no systematic study that allows to quantify these effects. The present article addresses this gap in knowledge by performing a systematic study of various micro-ramp geometries and relating the geometrical parameters to various measured features of the micro ramp wake by means of a simple physical model.

2. Flow features

The overall mean flow field downstream of the micro ramp contains various typical flow structures, notably the streamwise pair of (primary) counter-rotating vortices and secondary vortices (see Figure 1). Furthermore, behind the micro ramp a momentum deficit wake region is established, where the streamwise velocity is lower than the surrounding flow (see Figure 2). This results in a strong 3D shear layer which is responsible for the formation of hairpin/ring-shaped vortices due to the growth and roll-up of Kelvin-Helmholtz (K-H) instabilities. The K-H vortices do not actively contribute in the flow control, and also do not show up in the time-averaged representation of the flow field, but they affect the primary vortices by producing regions of local acceleration and deceleration and hereby modify the vorticity field of the primary vortices [7]. The primary vortices have a major contribution in the flow control mechanism which can be characterized and quantified by the circulation [6]. The effectiveness of a device in improving the boundary layer profile can be judged by measuring the velocity field in the symmetry plane as seen in Figure 2. The momentum deficit is stronger near the micro ramp and gets filled up downstream by the action of streamwise vortices. Furthermore due to the central upwash the wake lifts away from the wall. The momentum deficit region can be characterized by measuring the wake velocity, which is the minimum streamwise velocity in the symmetry plane at a given streamwise location. The wall normal location of the wake velocity is termed as the wake location. The response of these wake characteristics to changes in the geometrical parameters of the micro ramp is investigated in the present study.

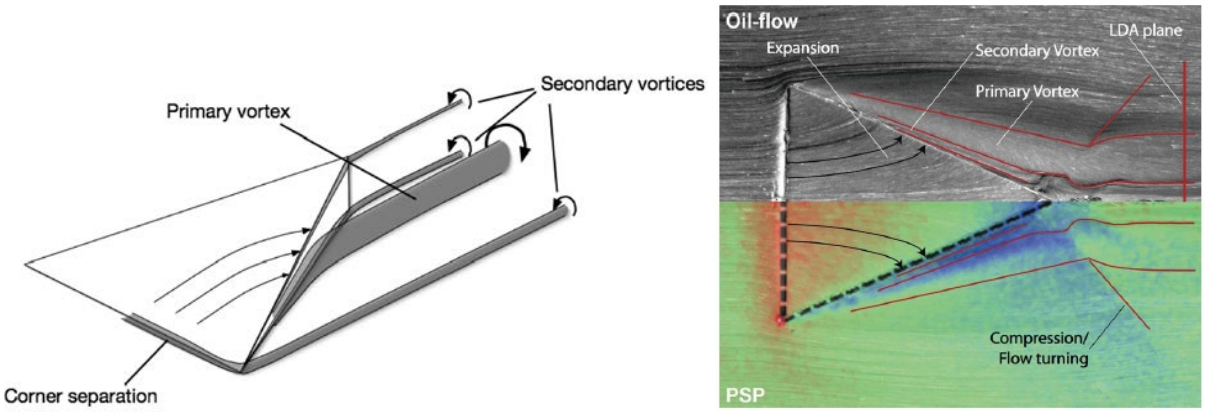

(a) (b)

Figure 1: Flow structures around the micro ramp. (a) A conceptual sketch representing the vortical structures [4]. (b) Oil flow and pressure sensitive paint measurements showing surface flow features, traces of vortices as well as the surface pressure distribution [6].

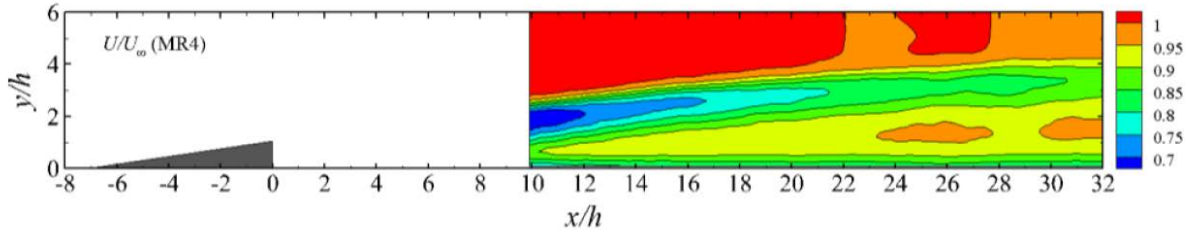

Figure 2: Contours of the time average of streamwise velocity in the symmetry plane of a micro ramp [7].

3. Experimental setup

A parametric study is conducted by systematically varying the parameters that define the micro ramp geometry. The flow field in the micro ramp wake is investigated by means of 2 component (2C) planar PIV in the symmetry plane of the micro ramp and 3 component (3C) stereo PIV at selected cross-flow planes.

3.1 Flow facility

Experiments are performed in the supersonic wind tunnel ST-15 at the Aerospace Engineering Faculty of TU Delft. The micro ramps are mounted on the wind tunnel floor for the PIV measurements and on the side walls for top view schlieren visualizations. The tunnel wall boundary layer is fully turbulent with a thickness of $\delta = 6\,mm$, as was measured by PIV. The free-stream Mach number is kept constant ($M_\infty = 2$) in the investigation. Detailed data of the experimental conditions is shown in the Table 1.

Table 1: Flow conditions and undisturbed boundary layer properties.

Property	**Value**
Free stream Mach number $\boldsymbol{M_\infty}$	2.0
Total temperature $\boldsymbol{T_o}$ $(\boldsymbol{K})$	266.5
Total pressure $\boldsymbol{P_o}$ $(\boldsymbol{N/m^2})$	3.15×10^5
Free stream velocity $\boldsymbol{U_\infty}$ $(\boldsymbol{m/s})$	487
Reynolds number based on height $\boldsymbol{Re_h}$	1.85×10^5
Friction velocity $\boldsymbol{u_\tau}$ $(\boldsymbol{m/s})$	19.5
Skin friction coefficient $\boldsymbol{C_f}$	1.9×10^{-3}
Incompressible momentum thickness $\boldsymbol{\theta_i}$ **(mm)**	0.524
Reynolds number based on momentum thickness $\boldsymbol{Re_{\theta_i}}$ $(\boldsymbol{1/m})$	46.2×10^6

3.2 Micro ramp configurations

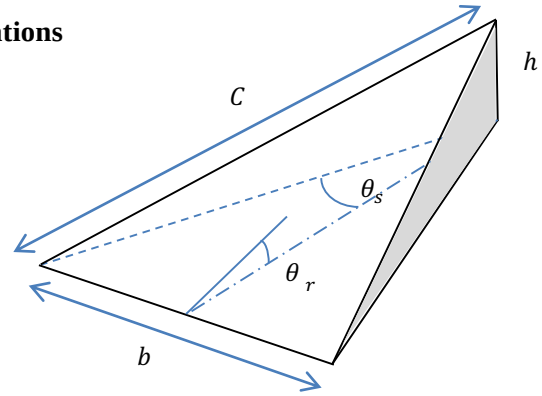

Figure 3: Micro ramp geometry

The most common micro ramp configuration considered by researchers is the one resulting from the optimization study conducted by Anderson [3], for which reason it is also referred to as the Anderson micro ramp. The flow field behind Anderson micro ramps has been explored in great detail in the literature [1], [3], [6], [7]. Therefore this configuration is chosen as the baseline configuration for the present study and other configurations are derived by varying each geometrical parameter at a time. The micro ramp geometry is parameterized using the following parameters: height (h), half span angle (θ_s) and ramp angle (θ_r) (see Figure 3). For all configurations the trailing edge of the micro ramp is perpendicular to the wall. Since the effect of varying micro ramp height has already been explored in the literature [9] and there is a multitude of other parameters to be considered, the micro ramp height is kept constant ($h = 4mm$, 67% of the boundary layer thickness) throughout the current study. The different test configurations in this study are obtained by varying θ_s (half span sweep) and θ_r (ramp sweep). A detailed test matrix is shown in the Table 2.

Table 2: Configuration matrix

Configuration	Height (h) mm	Half span angle (θ_s) °	Ramp angle (θ_r) °
MR24 (baseline)	4	24	8.64
MR20	4	20	8.64
MR28	4	28	8.64
MR36	4	36	8.64
MR45	4	45	8.64
MR4	4	24	4.3
MR6	4	24	6.45
MR11	4	24	11
MR21	4	24	21.3

3.3 PIV arrangement

The flow field in the symmetry plane $z/h = 0$ of the micro ramp is studied with 2C planar PIV, with the field of view ranging from $x/h = 6.5$ to 29 ($x/h = 0$ corresponds to the trailing edge). In addition, the flow field in the cross flow plane is measured using 3C stereo PIV at the streamwise locations $x/h = 5$ and $x/h = 15$. The flow is seeded with Di-Ethyl-Hexyl-Sebacate (DEHS) tracer particles. A double cavity Nd:YAG Spectra Physics Quanta Ray PIV-400 laser is used for the illumination. Specifications of the PIV setup are summarized in the Table 3.

Table 3: Specification of the PIV setup

	Planar PIV	Stereo PIV
Camera	3x Lavision imager LX (2M)	2x Lavision imager LX (2M)
Spatial resolution	39.9 px/mm	49.9 px/mm
Pulse separation dt (s)	1 μs	1 μs
Recording rate (Hz)	5.05	5.05
Free-stream particle displacement (mm)	0.5	0.5
Laser sheet orientation	Streamwise	Cross-flow
Laser sheet thickness (mm)	$1.4 - 2$	2.5

The commercial software DaVis 8.1.2 from LaVision is used for data acquisition and processing. First the particle images are pre-processed to minimize light reflections, by subtracting the time minimum from the individual snapshots. Effects of inhomogeneous illumination are compensated by dividing the snapshots by the average of the particle images. The vector calculation is carried out with a multi-pass approach. In the case of planar PIV, the window size is varied from 96 ×96 pixels (square, 50% overlap) to a final size of 32×32 pixels (elliptical 4:1, 75% overlap). In the case of stereo PIV the window size is varied from 64 ×64 pixels (square, 50% overlap) to a final size of 32×32 pixels (Circular, 75% overlap). These settings result in a vector pitch of 0.2 mm for the 2C PIV measurements and 0.16 mm for the stereo PIV measurements. For each test case a total of 400 PIV image pairs are recorded.

3.4 Uncertainty analysis

The various types of uncertainties involved in the present measurements are summarized in Table 4, the procedure to determine these uncertainties is outlined in [7]**.**

Table 4: Uncertainty analysis

Uncertainty parameter	Value
Statistical ε_u	$< 6.7\ m/s$
Statistical ε_v	$< 7.35\ m/s$
Cross-correlation ε_{cc}	$< 2.38\ m/s$
Spatial resolution $\Delta u/u_o$	$< 4\%$
Particle slip ε_{τ_p}	$< 3.15\ m/s$
Vorticity $\varepsilon_\omega h/U_\infty$	< 0.12

Apart from the uncertainties related to the measurement technique also practical uncertainties should be considered. Great care was taken to paste the micro ramp in the correct position using a template, however there may still be minor errors in the positioning effectively resulting in a small yaw angle. For the present experiments it is estimated that this is less than 1°. The laser sheet used for the PIV measurements has a thickness between 1.4 mm and 2 mm, and the measured flow field is an average over the light sheet thickness. This effect introduces the largest errors for the streamwise 2C PIV measurements where at the start of the measurement domain the width of the wake is small compared to the light sheet thickness.

4. Flow organization

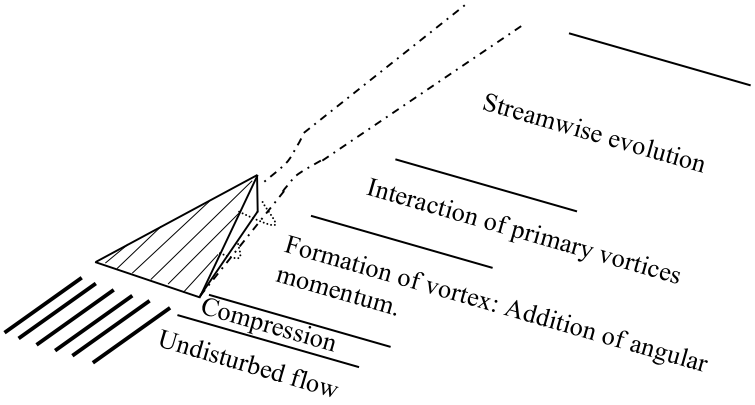

Figure 4: Evolution of the primary vortices around and downstream of the micro ramp

The incoming boundary layer undergoes compression when it encounters the leading edge of the micro ramp. The flow subsequently travels over the ramp surface and leaves at the micro ramp chord, which is the edge labelled as C in Figure 3. As seen in the Figure 1b, the flow on the micro ramp surface turns towards the chord before it separates. A low pressure region exists at the side of the micro ramp which leads towards the formation of the primary vortex. Also, part of the vorticity from the incoming boundary layer is transferred to the primary vortex. The vortices from the two sides of the micro ramp approach each other just downstream of the trailing edge where they form a vortex pair creating the mutual up-wash. Further downstream of the interaction zone, the cores of the primary vortices move apart from each-other as they grow in size and vorticity is diffused over a larger area. The mutual up-wash also results in the lift up of the vortices as well as of the momentum deficit region (wake). When they evolve downstream the primary vortices bring the higher momentum flow closer to the wall, which makes the boundary layer profile fuller.

Streamwise and wall normal velocity contours in the symmetry plane for the baseline configurations are shown in Figure 5. The momentum deficit region originates just downstream of the micro ramp and it gets filled up when moving in downstream direction (see Figure 5a). The lift up of the wake is also well captured. It can also be observed in Figure 5b that the mutual up-wash is stronger near the micro ramp and reduces further downstream. The flow field in the cross-flow planes is shown in Figure 6 with the contours of streamwise velocity where primary vortex cores are also observed. The boundary layer thickness is reduced beneath the cores as compared to the surrounding which is a direct indicator of the momentum addition near the wall. It is important to note that the highest momentum addition is observed right beneath the vortex cores and not in the symmetry plane (see Figure 6a). The wake is filled up and vortices decay at the further downstream location. Figure 7 shows the streamwise velocity profiles for different configurations at a fixed streamwise location (x/h = 10.8). The two inflection points in the profiles indicate the extent of the shear layer. Even though at this streamwise location the momentum addition phase of all the configurations is not yet complete, in some cases the velocity profile near the wall is already fuller than that of the undisturbed boundary layer. These cases include micro ramps with $\theta_s < 24^o$ or $\theta_r > 8.65^o$. Wall normal velocity profiles for different configurations are shown in the Figure 8. It is interesting to note that the ramp angle has a higher effect on the maximum up-wash velocity than the half span angle.

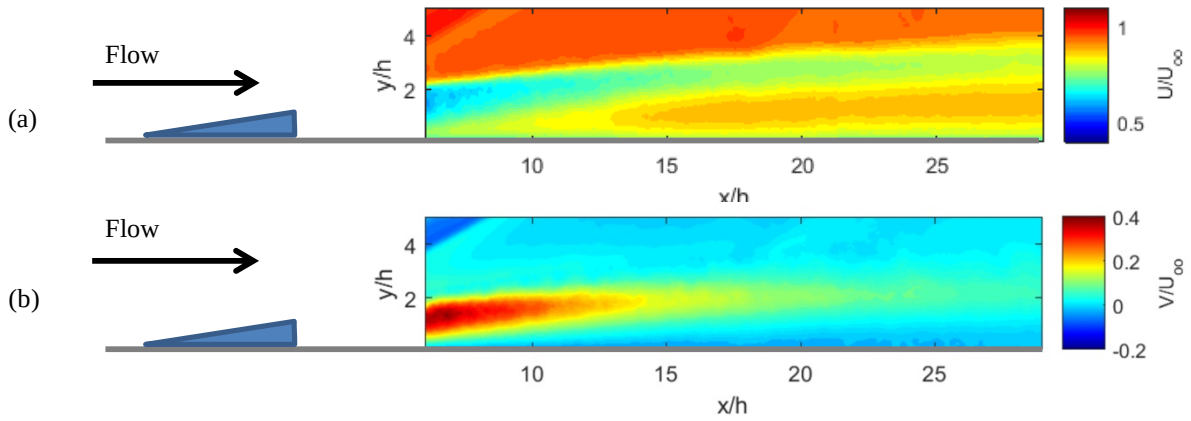

Figure 5: Contours of (a) streamwise velocity and (b) wall-normal velocity in the symmetry plane of the micro ramp as measured with PIV. (Baseline configuration, MR24)

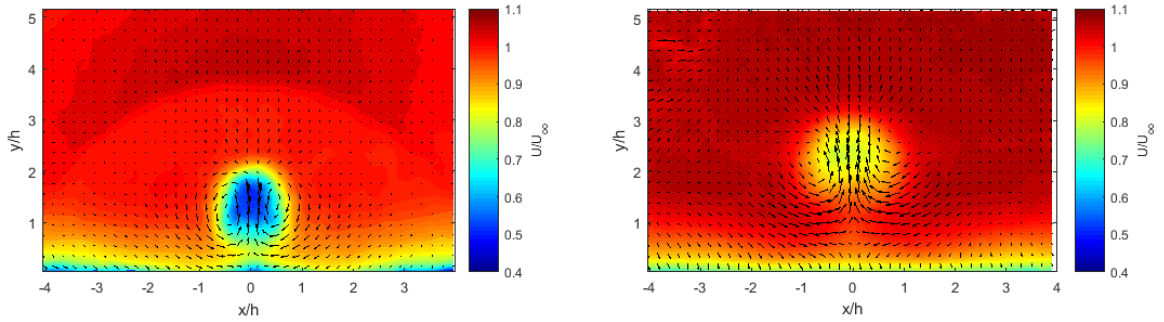

Figure 6: Flow field in the cross-flow planes with the contours of streamwise velocity at (a) $x/h = 5$ and (b) $x/h = 15$. (Baseline configuration)

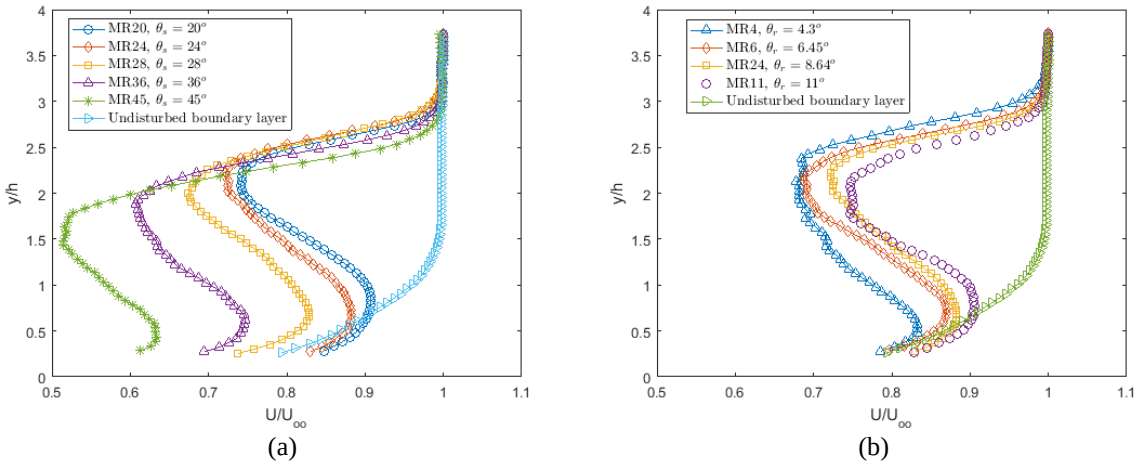

Figure 7: Streamwise velocity profiles measured at $x/h = 10.7$; (a) half span angle sweep (b) ramp angle sweep

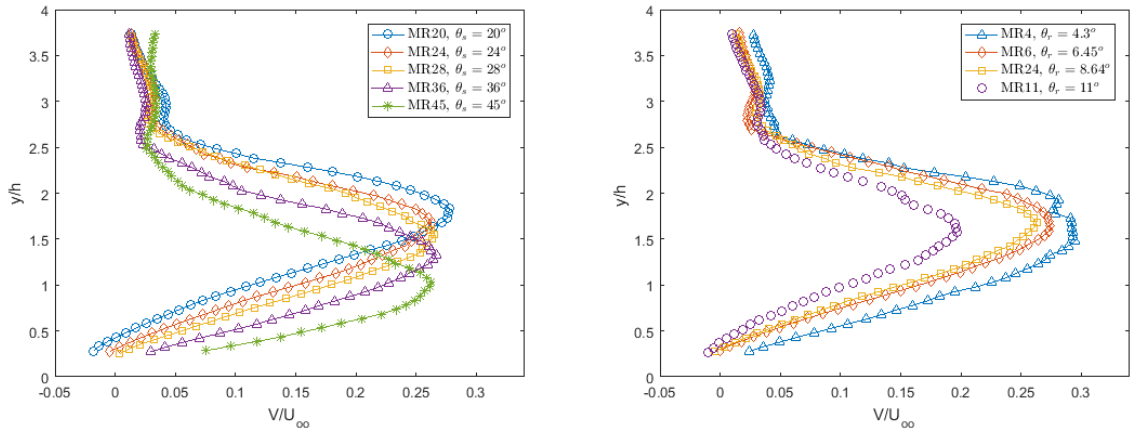

(a) (b)

Figure 8: Wall normal velocity profiles measured at $x/h = 10.7$; (a) half span angle sweep (b) ramp angle sweep

4.1 Wake velocity

The streamwise evolution of the wake velocity, which is the minimum streamwise velocity in the wake, is useful to assess the effectiveness of the primary vortices in filling up the wake. For similar incoming flow conditions, a lower wake velocity indicates a higher momentum deficit and hence higher drag. As shown in Figure 9, it is observed that for every configuration, the wake velocity is low at first and gradually increases with the streamwise distance. The non-dimensional wake velocity approaches values ranging from 0.75 – 0.85 within the measurement domain depending on the exact geometry. It appears that the wake velocity decreases with increasing half span angle or with decreasing ramp angle, irrespective of the streamwise location. .

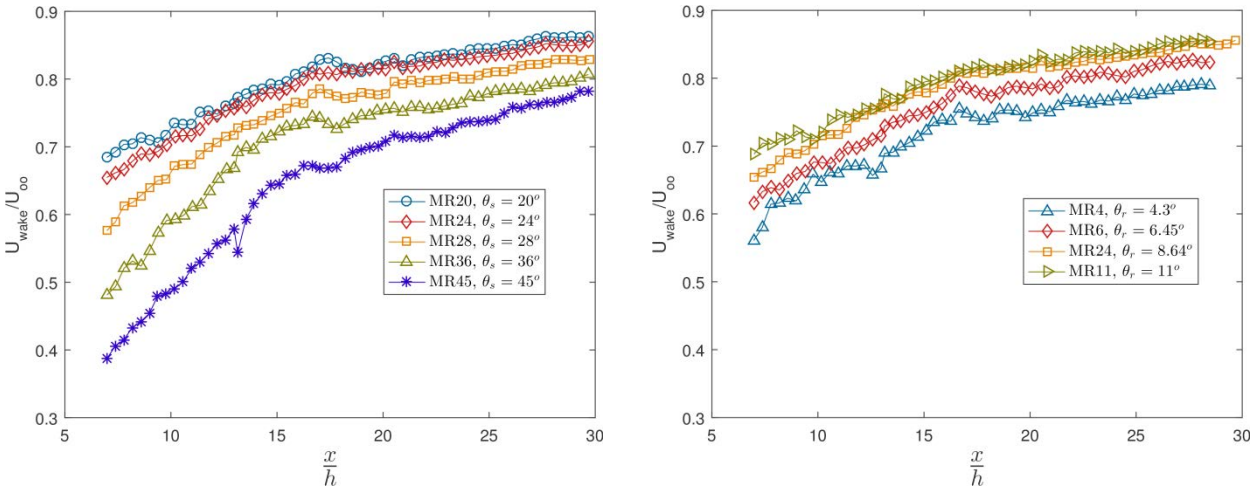

(a) (b)

Figure 9: Streamwise evolution of wake velocity for (a) half span angle sweep and (b) ramp angle sweep.

4.2 Wake location

The streamwise evolution of wake location, which is the wall-normal location of where the wake velocity occurs, represents the wake trajectory. Furthermore, based on tomographic PIV investigations, Sun [7] observed that the wall normal location of the primary vortex cores is very close to the wake location. This has also been confirmed in the present study. Hence, the wake location is a useful measure of the trajectory of the primary vortex cores. Figure 10 shows the wake trajectories for all configurations, which reflect the upward migration induced by the upwash of the primary vortex pair. The evolution of wake location shows a significant variation for the half span angle sweep (Figure 10a). For the higher half span angle the wake remains closer to the wall, which can be linked with the increased core separation and reduced mutual up-wash (see Figure 12). The wake location does not seem to be significantly affected by variations in the ramp angle (Figure 10b).

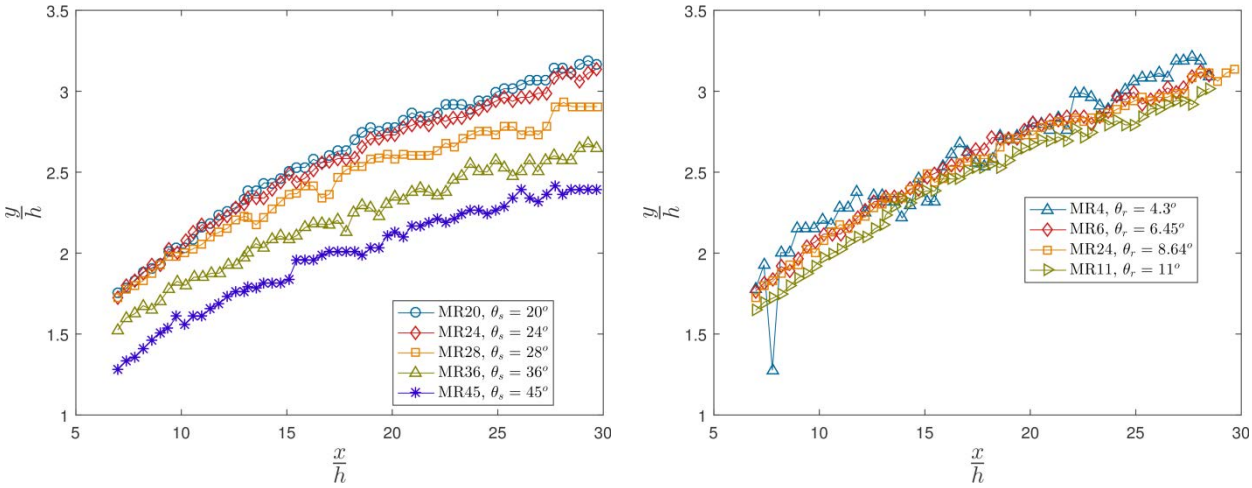

(a) (b)

Figure 10: Streamwise evolution of wake location. (a) half span angle sweep (b) ramp angle sweep.

4.3 Core separation

The span-wise distance between two primary vortex cores is termed as the core separation. A top-view of the wake of the micro ramp is obtained from the schlieren measurements and the vortex core is traced from the images (see Figure 11). Near the micro ramp trailing edge, the core separation is more sensitive to the changes in the half span angle than the changes in the ramp angle. The increased core separation in the case of ramp angle sweep can be related to the increased core size and a stronger vortex. This is also evident from the corresponding increase in the mutual upwash (Figure 8b). However, when the half span angle is increased, the vortex core leaves the micro ramp chord earlier and meets the vortex from the other side at a further downstream location (see Figure 12).

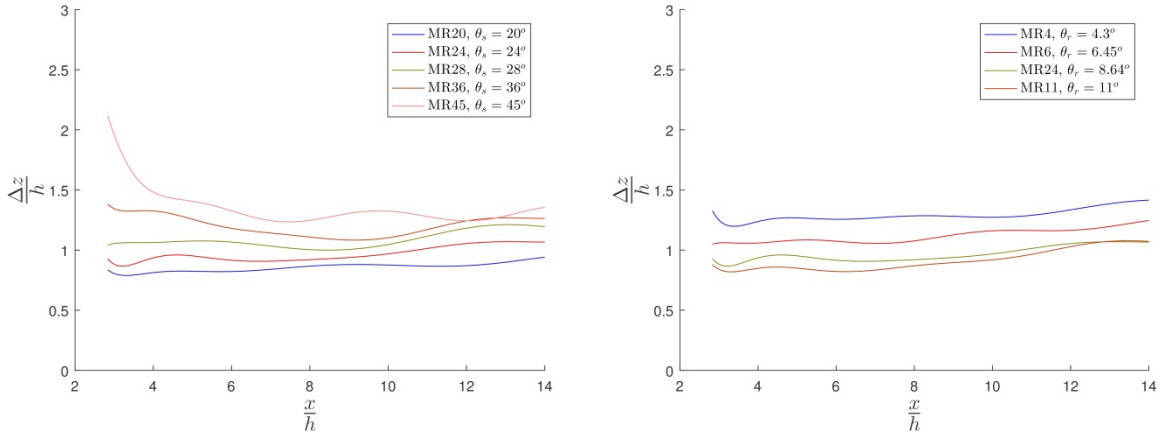

(a) (b)

Figure 11: Primary vortex core separation vs streamwise coordinate.

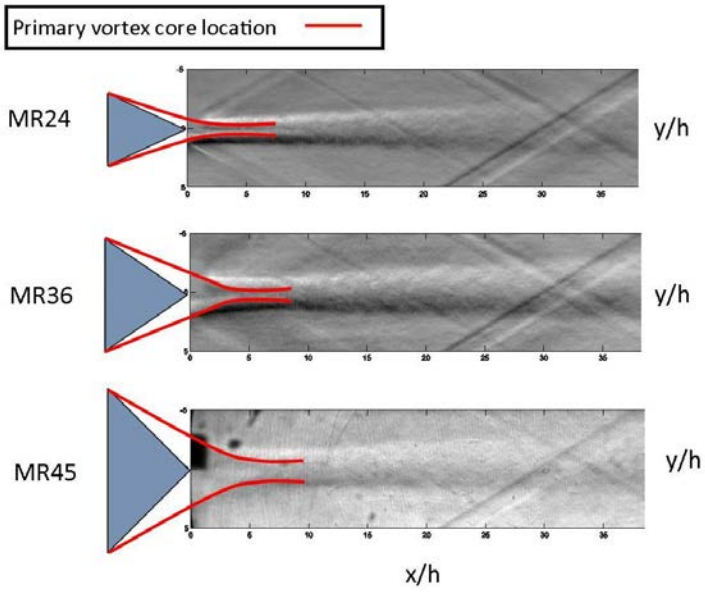

Figure 12: Effect of larger half span angle on the core separation.

4.4 Incompressible added momentum

The effectiveness of the micro ramp in flow control authority can be judged based on the amount of momentum added in the near-wall region. Giepman et al. [9] found that the shock induced separation bubble is sensitive mainly to the boundary layer momentum below $0.5\delta_{99}$. Therefore to quantify the effectiveness of a micro ramp Giepman et al. introduced the concept of (incompressible) added momentum in the symmetry plane of the micro ramp:

$$E_{added} = \int_0^{0.5\delta_{99}} \frac{U^2 - U_{clean}^2}{U_\infty^2}\, dy \tag{1}$$

Here, U_{clean} corresponds to the velocity profile of the undisturbed boundary layer. Streamwise evolution of the incompressible added momentum for different configurations is shown in the Figure 13. It is observed that up to around $x/h = 17$ momentum is being added to the boundary layer. After this location the added momentum reaches a plateau. It is observed that for the higher ramp angles and lower span angles, the added momentum in the symmetry plane is overall higher.

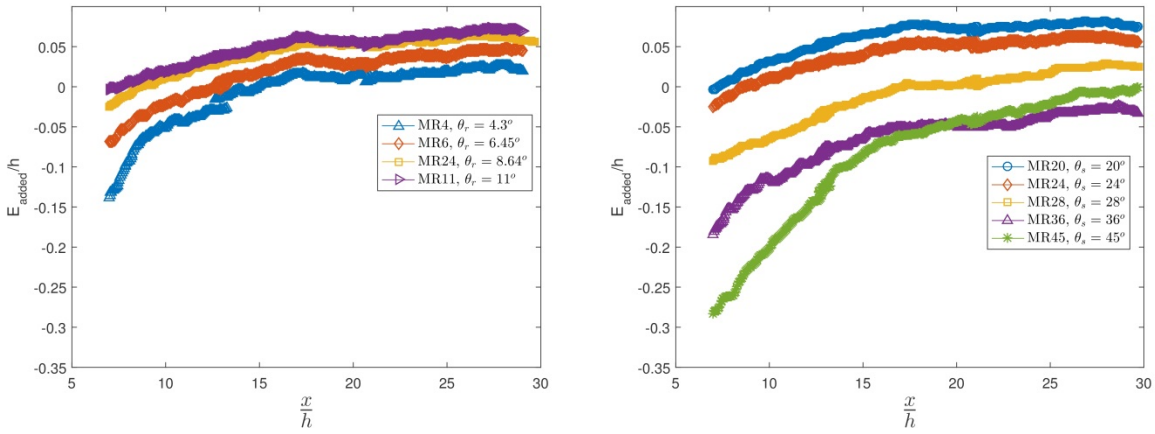

(a) (b)

Figure 13: Streamwise evolution of incompressible added momentum measured in the symmetry plane (a) ramp angle sweep (b) half span angle sweep

5. Physical model

Using information from literature and the present experiments a simple physical model of the flow field is created to describe the flow properties in the micro ramp wake. Furthermore, using this model a new scaling is proposed (and validated) that takes into account the effect of the geometrical features on the flow field in the wake.

5.1 Central concept

The micro ramp is a passive device that redistributes the momentum in the oncoming flow in order to create streamwise vorticity in its wake. The primary vortices are responsible for the mixing and subsequent filling of the wake, whereas, the drag of the device and secondary features like K-H vortices depends on the momentum deficit region. The strength of the primary vortices and the flow characteristics of the momentum deficit depends on the amount of the total momentum in the flow on which the micro ramp is acting. This momentum which faces the micro ramp leading edge is defined here as the 'captured momentum'. Considering one half of the micro ramp geometry, this momentum is partially carried over to a single vortex and hence is proportional to the half span length $b/2$ of the micro ramp. Figure 14 illustrates the relation of the captured momentum with the micro ramp geometry.

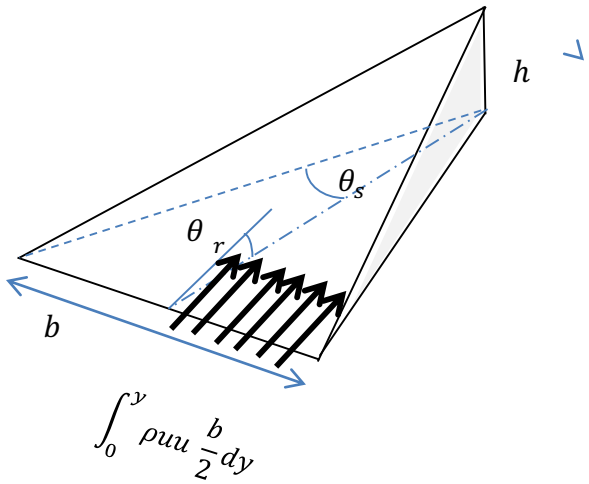

Figure 14: Concept of captured momentum

The length of the half span can be expressed in terms of the half span angle, ramp angle and micro ramp height:

$$\frac{b}{2} = h\frac{tan(\theta_s)}{tan(\theta_r)}. \tag{2}$$

And thus the captured momentum (P_c) can be written as:

$$P_c = \int_0^y \rho uu\frac{b}{2}dy = h\frac{tan\,(\theta_s)}{tan(\theta_r)}\int_0^y \rho uu\,dy. \tag{3}$$

Note that the factor $h\tan(\theta_s)/tan(\theta_r)$ represents how the captured momentum changes with variations in any of the geometrical parameters of the micro ramp. However, it is also important to note that the second part in equation (3) depends upon the incoming boundary layer profile. Hence, for similar upstream flow conditions, the half span length, $b/2 = h\tan(\theta_s)/tan(\theta_r)$, can be used for the scaling of the various characteristics of the micro ramp wake.

5.2 Circulation of primary vortex

The circulation of a primary vortex can be related to the geometrical parameters by a simplified conceptual analysis of the vortex formation. For this purpose, it is assumed that the stream-tubes over the micro ramp surface leave the micro ramp edge without undergoing any span-wise turning. Thus the streamwise velocity can be decomposed into a component normal and a component parallel to the micro ramp chord, see Figure 15a. The normal component $Usin(\theta_s)$ has a major contribution towards the formation of the primary vortex, while the parallel component,

$Ucos(\theta_s)$ does not contribute to the primary vortex directly. Figure 15b shows that the normal velocity component, $Usin(\theta_s)$, is being added as the tangential velocity component in the primary vortex throughout the length of the chord.

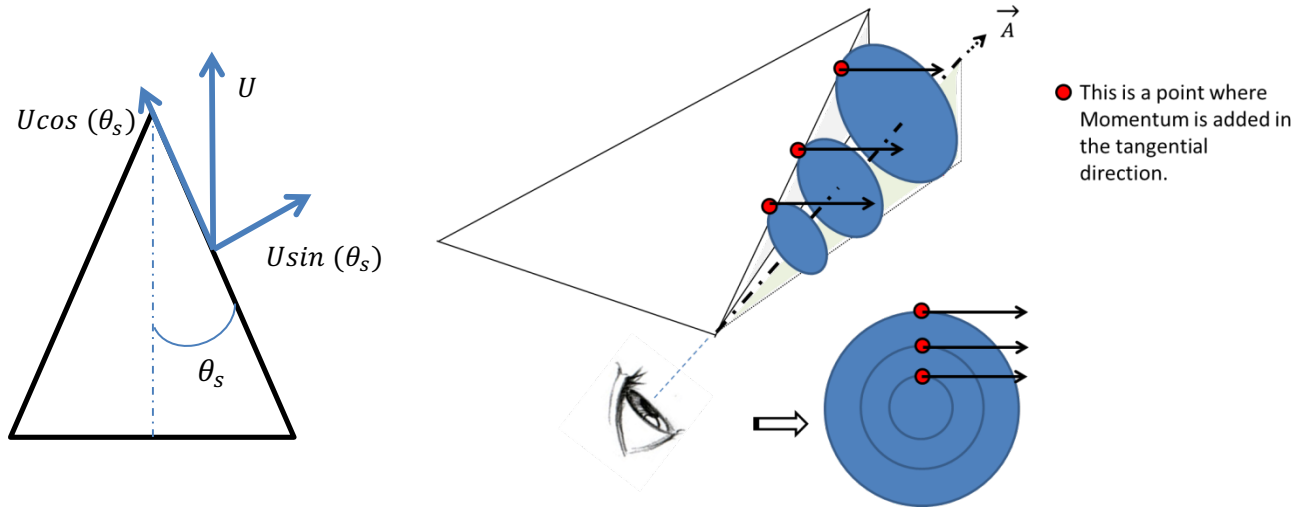

(a) (b)

Figure 15: Primary vortex formation: (a) Decomposition of the streamwise momentum in tangential and chord-wise direction. (b) Addition of the tangential momentum at various chord-wise locations.

When viewed along the axis of the primary vortex, this would seem like there is a constant addition of the tangential momentum at each radial location. Therefore, it can be assumed that for a larger length of the chord, a higher amount of tangential momentum is added to the vortex. Hence, the effective radius of the vortex at the trailing edge of the micro ramp can be assumed to be proportional to the length of the chord C, hence:

$$R = K_R C = K_R \frac{h}{cos(\theta_s)\,(tan(\theta_r)} \left(1 + \frac{(tan(\theta_r)\,cos(\theta_s))^2}{2}\right) \tag{4}$$

Here, K_R is a proportionality parameter, while furthermore the chord length has been expressed in terms of the geometrical parameters of the micro ramp. With this, the circulation at the end of the trailing edge can be written as follows:

$$\Gamma_{TE} = 2\pi U sin(\theta_s) R = K_R 2\pi U h \frac{tan(\theta_s)}{tan(\theta_r)} \left(1 + \frac{(tan(\theta_r)\,cos(\theta_s))^2}{2}\right) \tag{5}$$

Equation (5) represents the circulation of a primary vortex at the trailing edge of the micro ramp. However, it is known from literature [6], [7], [10] that the circulation scales with the micro ramp height and the friction velocity. This scaling is therefore incorporated into equation (5), yielding:

$$\frac{\Gamma_{TE}}{u_\tau h} = K_{circ} 2\pi \frac{tan(\theta_s)}{tan(\theta_r)} \left(1 + \frac{(tan(\theta_r)\,cos(\theta_s))^2}{2}\right) \tag{6}$$

Where $K_{circ} = K_R U/u_\tau$. Note that U is the average velocity of the fraction of boundary layer which enters into the primary vortex core. The exact value of U depends on the maximum wall normal coordinate up to which the momentum is captured by the micro ramp. This is not directly known but is incorporated into the semi-empirical

parameter K_{circ}. Finally, for a certain streamwise location (x/h) the value of circulation can be represented by introducing a parameter K_1, which depends on the streamwise location.

$$\frac{\Gamma_{x/h}}{u_\tau h} = K_{circ} 2\pi \frac{tan(\theta_s)}{tan(\theta_r)} \left(1 + \frac{(tan(\theta_r)\, cos(\theta_s))^2}{2}\right) + K_1(x,h) \qquad (7)$$

6. Model validation

6.1 Wake velocity

In various studies, the micro ramp height is used as the length scale to nondimensionalize the wake properties. Giepman et al. 2013 tested the Anderson micro ramp with different device heights and found that the graphs of streamwise evolution of the wake velocity collapse when the streamwise coordinate is scaled with the device height. They also found that the same scaling can be used for the added incompressible momentum. However, in the present study the device height is kept constant and still a significant difference in the wake velocity evolution is observed for different half span and ramp angles (see Figure 9). This suggests that apart from the micro ramp height also other parameters have an important effect on the scaling of the wake properties.

Since it was before postulated that the wake behaviour strongly depends on the captured momentum, the geometry term $h\tan(\theta_s)/tan(\theta_r)$ instead of h is used as non-dimensionalization factor. The results for the wake velocity, reported in Figure 9, all collapse onto a single curve when scaled with the new geometry term, see Figure 16. This therefore provides a first indication that the captured momentum concept indeed makes sense when describing the wake dynamics. However, the exact mechanism of this dependence is still to be explored.

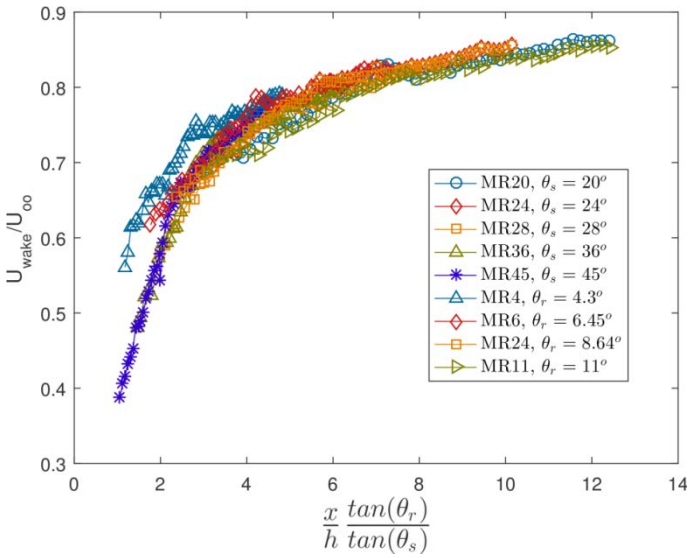

Figure 16: Streamwise evolution of wake velocity with the present scaling.

6.2 Wake location

The evolution of the wake location does not scale as good with the newly introduced scaling factor, see Figure 17. The effect of the new scaling is strong in the case of half span angle sweep however also for the ramp angle sweep the present scaling results in plots being further apart. This was to be expected since from Figure 10b it can be observed that the wake location evolution is not affected strongly by the variations in the ramp angle. It is clear from the wall normal velocity profiles (see Figure 8), that the decreasing ramp angle results in an increasing up-wash in the symmetry plane. There is also an increase in the vortex core separation (see Figure 11) which should have resulted in a lower wake location. Apparently this effect is compensated by the increased up-wash hence the wake location stays nearly the same. However, when the half span angle is increased, the core separation increases. But the up-wash remains nearly the same and it can no longer compensate for the increased core separation. As a result the wake location is lower and shows strong dependency on the half span angle.

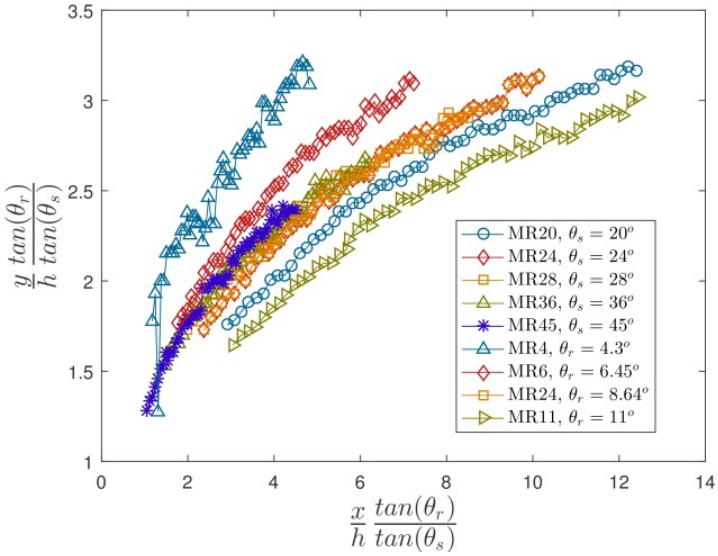

Figure 17: Streamwise evolution of wake location scaled with the present scaling factor

6.3 Circulation of the primary vortex pair

The flow field measurements in the cross-flow planes (at $x/h = 5$) are used to calculate circulation of the primary vortices for the different configurations. Equation (8) is fitted to the measured circulation of the 4 configurations in the ramp sweep ($\theta_r = 6.45^o \; to \; 21.3^o$) and values of parameters $K_{circ} = 0.8729$ and $K_1 = 4.433$ are determined. This expression is then compared to the circulation obtained for the other configurations (that were not used in the fit). The fit is found to be in good agreement with the experimental data for the half span angles within $\theta_s = 20^o \; to \; 28^o$ and for the ramp angles within $\theta_r = 6.45^o \; to \; 21.3^o$, see Figure 18.

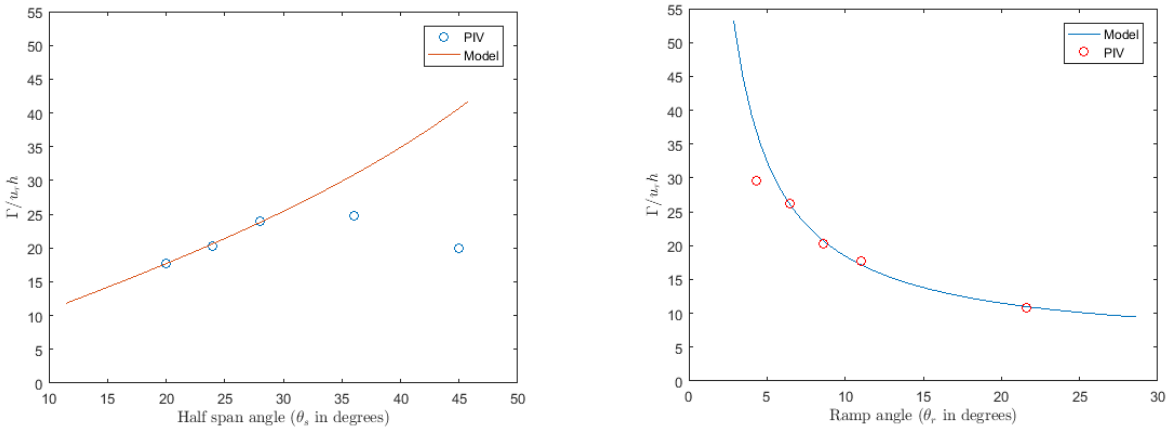

(a) (b)

Figure 18: Circulation of the primary vortices at x/h=5 for all the configurations.

A deviation from the fit is observed for the micro ramps with higher half span angles and lowest ramp angles. For the higher half span angles the vortex core leaves the micro ramp chord earlier (see Figure 12). As a result, lower amount of captured momentum goes into the vortex core. Also, larger separation between two vortex cores delays the formation of the mutual up-wash further downstream. Due to the absence of mutual up-wash just downstream of the trailing edge, the cores stay closer to the wall where the viscous effects may lead to the lower values of circulation. A similar argument is true in the case of the lower ramp angles. The core separation increases with decreasing ramp angle and also with increasing half span angle (see Figure 11).

Equation (5) suggests that the half span length of the micro ramp, $b/2 = h\tan(\theta_s)/tan(\theta_r)$, has a significant effect on the primary vortex circulation. To further substantiate this, the circulation is plotted against the half span length (see Figure 19). It can be observed that the values of circulation are similar for the micro ramps with similar span length, even for different geometrical configurations. Physically this confirms that the vortex strength is directly dependent on the amount of captured momentum and how this momentum is distributed to the vortex core. Deviations from this trend are again observed for the higher half span angles and low ramp angle.

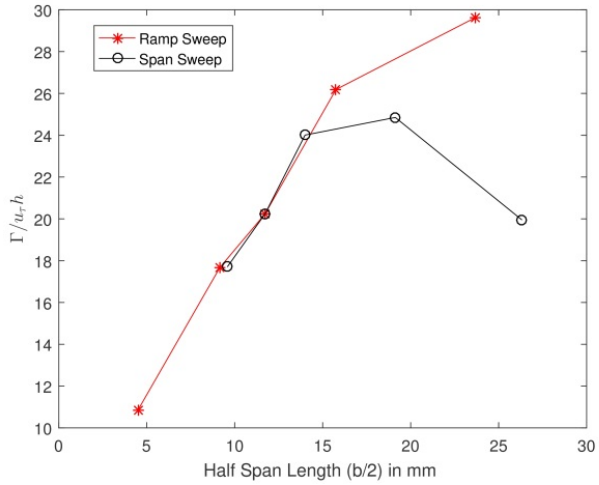

Figure 19: Effect of half span length on the normalized circulation of primary vortices.

6.4 Incompressible added momentum

In the case of ramp angle sweep, the streamwise evolution of the incompressible added momentum properly scales with the present scaling, however, it does not scale in the case of the half span angle sweep (see Figure 20). This can again be linked to the higher core separations for larger half span angles (see Figure 12). In the case of the half span sweep, with an increased core separation vortex cores stay closer to the wall (see Figure 10a). When the vortex core is away from the symmetry plane and closer to the wall, its effectiveness in bringing high momentum fluid from the surrounding flow towards the symmetry plane reduces. This results in the lower value of the added incompressible momentum. In the case of ramp angle sweep, the core separation increases with decreasing ramp angle. But the location of vortex core is also a bit higher (see Figure 10b). This results in the effective addition of momentum in the symmetry plane.

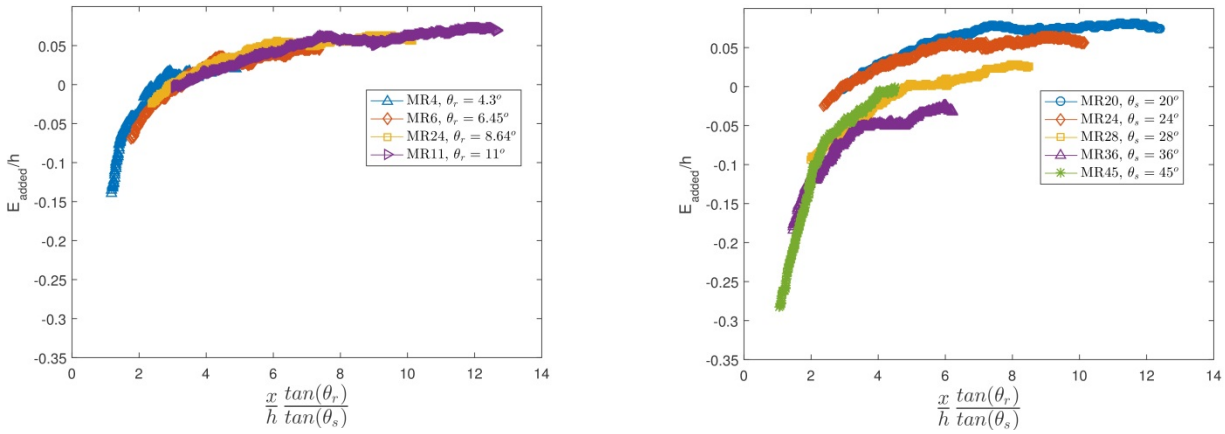

(a) (b)

Figure 20: Streamwise evolution of the added incompressible momentum with present scaling. (a) half span angle sweep (b) ramp angle sweep

7. Conclusion

The physical relation between micro ramp geometry and the downstream flow topology is investigated by means of a parametric study. The micro ramp geometry is parameterized with 3 parameters: height (h), half span angle (θ_s) and ramp angle (θ_r). The test configurations are derived by varying the latter two and keeping the device height constant throughout the study. For the same device height, changes in the half span angle or ramp angle are found to have significant effect on the flow topology. Increasing half span angle or decreasing ramp angle have similar effects on the flow characteristics of the micro ramp wake. These effects include: decreased wake velocity, larger core separation and lower incompressible added momentum. However, the mutual up-wash of the two primary vortices is more sensitive to the changes in ramp angle. It increases with the lowering of ramp angle but remains nearly the same with the changes in half span angle. With increasing half span angle the vortex core leaves the micro ramp chord earlier, this behaviour is not observed when the ramp angle is changed. In order to provide a physical reasoning to the observed effects, a physical model is formed. This model includes the concept of captured momentum, a mechanism to relate the geometry to the vortex circulation and leads to a new geometrical scaling. Since the micro ramp is a passive device, its working mechanism to generate streamwise vorticity largely depends on re-distributing the momentum in the incoming flow. The momentum which faces the micro ramp chord is partly transferred into the primary vortices. This momentum is referred to here as the captured momentum and it governs the flow characteristics of the micro ramp wake. For similar incoming flow conditions, the captured momentum corresponding to one primary vortex, is directly proportional to the half span length of the micro ramp. Hence, the half span length is used as a length scale for scaling of different flow characteristics of the micro ramp wake. It is found that the plots of wake velocity evolution collapse on a single curve when the streamwise coordinate is scaled with the half span length. A similar scaling effect is observed in the added incompressible momentum for the cases in ramp angle sweep. In the case of the half span angle sweep, the scaled plots shift downwards with the increasing half span angle, suggesting the decreasing effectiveness in momentum addition at the symmetry plane. This is linked to the increased separation of the primary vortex cores as the span angle increases. The wall-normal wake location scales with the half span length only in the case of the half span angle sweep, but does not depend strongly on the ramp angle. Based on the conceptual model, a simplified relation between primary vortex circulation and geometry parameters is formulated in this study. This relation still contains empirical parameters, but once these are determined for the flow conditions under consideration, a valid correlation is provided for half span angles within $\theta_s = 20^o \; to \; 28^o$ and for the ramp angles within $\theta_r = 6.45^o \; to \; 21.3^o$.

References

[1] R. H. M. Giepman, A. Srivastava, F. F. J. Schrijer, and B. W. van Oudheusden, “Mach and Reynolds number effects on the wake properties of microramps,” *AIAA Journal*, vol. 54, pp. 3481-3494, 2016.

[2] P. R. Ashill, J. L. Fulker, and K. C. Hackett, “Studies of Flows Induced by Sub-Boundary Layer Vortex Generators (SBVGs),” *AIAA-2002-0968*, 2002.

[3] B. H. Anderson, J. Tinapple, and L. Surber, “Optimal Control of Shock Wave Turbulent Boundary Layer Interactions Using Micro-Array Actuation,” *AIAA-2006-3197*, 2006.

[4] H. Babinsky, Y. Li, and C. W. PittFord, “Micro-ramp control of supersonic oblique shock-wave boundary-layer interactions,” *AIAA Journal*, vol. 47, pp. 668–675, 2009.

[5] A. G. Panaras and F. K. Lu, “A Micro-vortex generators for shockwave boundary layer interactions,” *Prog. Aerosp. Sci.* 74, pp.16–47, 2015.

[6] W. R. Nolan and H. Babinsky, “Characterization of Micro-vortex Generators in Supersonic Flows,” *AIAA-2011-71*, 2011.

[7] Z. Sun, “Micro Ramps in Supersonic Turbulent Boundary Layers: An experimental and numerical study,” *PhD Thesis*, TU Delft, 2014.

[8] Q. Li and C. Liu, “Implicit LES for Supersonic Micro ramp Vortex Generator: New Discoveries and New Mechanisms,” *Model. Simul. Eng.*, vol. 2011, Article ID 934982, 2011.

[9] R. H. M. Giepman, F. F. J. Schrijer, and B. W. van Oudheusden, “Flow control of an oblique shock wave reflection with micro-ramp vortex generators: Effects of location and size,” *Phys. Fluids*, vol. 26, Article number 066101, 2014.

[10] R. Giepman, “Flow control for oblique shock wave reflections,” *PhD Thesis*, TU Delft, 2016.